

## Samurai project: Verifying the consistency of black-hole-binary waveforms for gravitational-wave detection

Mark Hannam,<sup>1</sup> Sascha Husa,<sup>2</sup> John G. Baker,<sup>3</sup> Michael Boyle,<sup>4,5</sup> Bernd Brügmann,<sup>6</sup> Tony Chu,<sup>4</sup> Nils Dorband,<sup>7</sup> Frank Herrmann,<sup>8,9</sup> Ian Hinder,<sup>7,9</sup> Bernard J. Kelly,<sup>3</sup> Lawrence E. Kidder,<sup>5</sup> Pablo Laguna,<sup>9,10</sup> Keith D. Matthews,<sup>4</sup> James R. van Meter,<sup>3,11</sup> Harald P. Pfeiffer,<sup>4</sup> Denis Pollney,<sup>7</sup> Christian Reisswig,<sup>7</sup> Mark A. Scheel,<sup>4</sup> and Deirdre Shoemaker<sup>9,10</sup>

<sup>1</sup>*Physics Department, University College Cork, Cork, Ireland*

<sup>2</sup>*Departament de Física, Universitat de les Illes Balears, Cra. Valldemossa Km. 7.5, Palma de Mallorca, E-07122 Spain*

<sup>3</sup>*Gravitational Astrophysics Laboratory, NASA Goddard Space Flight Center, 8800 Greenbelt Road, Greenbelt, Maryland 20771, USA*

<sup>4</sup>*Theoretical Astrophysics 130-33, California Institute of Technology, Pasadena, California 91125, USA*

<sup>5</sup>*Center for Radiophysics and Space Research, Cornell University, Ithaca, New York 14853, USA*

<sup>6</sup>*Theoretical Physics Institute, University of Jena, 07743 Jena, Germany*

<sup>7</sup>*Max-Planck-Institut für Gravitationsphysik, Am Mühlenberg 1, 14475 Potsdam, Germany*

<sup>8</sup>*Center for Scientific Computation and Mathematical Modeling, University of Maryland, 4121 CSIC Building 406, College Park, Maryland 20742, USA*

<sup>9</sup>*Center for Gravitational Wave Physics, Pennsylvania State University, University Park, Pennsylvania 16802, USA*

<sup>10</sup>*Center for Relativistic Astrophysics, School of Physics, Georgia Institute of Technology, Atlanta, Georgia 30332-0430, USA*

<sup>11</sup>*Center for Space Science & Technology, Physics Department, University of Maryland Baltimore County, 1000 Hilltop Circle, Baltimore, Maryland 21250, USA*

(Received 20 January 2009; published 17 April 2009)

We quantify the consistency of numerical-relativity black-hole-binary waveforms for use in gravitational-wave (GW) searches with current and planned ground-based detectors. We compare previously published results for the ( $\ell = 2, |m| = 2$ ) mode of the gravitational waves from an equal-mass nonspinning binary, calculated by five numerical codes. We focus on the  $1000M$  (about six orbits, or 12 GW cycles) before the peak of the GW amplitude and the subsequent ringdown. We find that the phase and amplitude agree within each code's uncertainty estimates. The mismatch between the ( $\ell = 2, |m| = 2$ ) modes is better than  $10^{-3}$  for binary masses above  $60M_{\odot}$  with respect to the Enhanced LIGO detector noise curve, and for masses above  $180M_{\odot}$  with respect to Advanced LIGO, Virgo, and Advanced Virgo. Between the waveforms with the best agreement, the mismatch is below  $2 \times 10^{-4}$ . We find that the waveforms would be indistinguishable in all ground-based detectors (and for the masses we consider) if detected with a signal-to-noise ratio of less than  $\approx 14$ , or less than  $\approx 25$  in the best cases.

DOI: [10.1103/PhysRevD.79.084025](https://doi.org/10.1103/PhysRevD.79.084025)

PACS numbers: 04.25.D-, 04.20.Ex, 04.30.Db, 95.30.Sf

### I. INTRODUCTION

Direct detection of gravitational waves (GWs) is expected in the next few years by a network of ground-based laser-interferometric detectors, LIGO [1–3], Virgo [4,5], and GEO [6–8], which operate in the frequency range  $\sim 10^1$ – $10^4$  Hz. The scientific scope of gravitational-wave observations will be extended (see [9] for a recent overview) by space-based instruments such as LISA [10,11], which will be sensitive to signals at significantly lower frequencies. A likely source for the first detection, and an essential part of the science objectives of all gravitational-wave detectors, is the merger of black-hole-binary systems. Detection of gravitational-wave events and their further analysis rely on the theoretical modeling of waveforms. Until recently, theoretical waveforms for the coalescence of black holes were based on analytic approximations to the full general theory of relativity, in particular, the post-

Newtonian (PN) expansion, which models the signal from the slow inspiral of the two black holes, and black-hole perturbation theory, where the complex ringdown frequencies of black holes can be computed (see [12,13] for reviews). These methods cannot currently model, from first principles, the merger phase, when the wave amplitude peaks. Correspondingly, data-analysis methods so far had to be developed without information from complete black-hole-binary waveforms.

The situation changed with breakthroughs in numerical relativity (NR) in 2005 [14–16] that made it possible to calculate the late inspiral, merger, and ringdown of a black-hole-binary system in full general relativity, and to calculate the gravitational waves produced in the process. Since that time, many more numerical simulations have been performed [17–77], and efforts have been made to produce waveform templates based on numerical results [39,78–80]. Some of these template banks are already available to

be used for searches within the LSC Algorithm Library [81]. There is also an ongoing project to test search pipelines with injections of numerical data into simulated LIGO and Virgo noise, the Numerical INjection Analysis (NINJA) project [82]. The work described in this paper was conceived as complementary to that in the NINJA effort, and has subsequently been dubbed the Samurai project.

If waveform template banks based (at least in part) on numerical results are to be confidently used in detector searches, it is important to know the accuracy of the input numerical waveforms. Most numerical waveforms are published with some internal error analysis and uncertainty estimates. However, our goal in this paper is to perform a stronger consistency check by comparing the results of *different* numerical codes, produced using different formulations of the Einstein equations, initial data, gauge conditions, and numerical techniques. First studies comparing numerical waveforms were performed in [83,84]; our project extends those earlier works.

This paper serves two purposes: (1) to verify that the numerical waveforms we compare agree with each other within the uncertainty estimates originally published with those waveforms, and (2) to quantify the differences between the waveforms in terms and measures meaningful to both the numerical-relativity and gravitational-wave data-analysis communities. In particular, in addition to making a direct comparison between the phase and amplitude of the respective waveforms, we also compute their mismatch with respect to the Enhanced LIGO, Advanced LIGO, Virgo, and Advanced Virgo detectors, and the maximum signal-to-noise ratio (SNR) below which these waveforms would be indistinguishable.

In the present comparison we focus on the physical system that has been studied in the most detail by the numerical-relativity community: a binary consisting of equal-mass, nonspinning black holes following noneccentric inspiral and merger. Specifically, we consider the dominant ( $\ell = 2, |m| = 2$ ) spherical-harmonic mode, which has been the focus of most data-analysis research to date, and is the most important from the point of view of GW detection. It is now known that the subdominant modes are also important for parameter estimation, but we will leave an analysis of those to future work; see also our comments in the Conclusion. In order to keep the data-analysis aspects of this paper straightforward, we will discuss only single detectors, and neglect the subtleties introduced when dealing with networks of detectors or with time-delay interferometry.

We will consider the waveform from roughly  $1000M$  before merger to about  $80M$  after merger, where  $M$  is the total binary mass in geometrical units. This is about six orbits before merger, or  $0.005(M/M_\odot)$  seconds, where  $M_\odot = 1.477 \times 10^3$  m is the mass of the Sun.

We make use of results from the BAM [84,85], CCATIE [51], Hahndol [86,87], and MayaKranc codes [37],

which all use the Baumgarte-Shapiro-Shibata-Nakamura (BSSN)/moving-puncture [15,16,87–92] approach and finite-difference techniques, and the  $\text{SpEC}$  code [22], which solves a variant of the generalized-harmonic system [30,93,94] using pseudospectral methods.

The paper is organized as follows. In Sec. II we summarize the numerical waveforms that we analyze, and the codes that were used to produce them. In Sec. III we directly compare the phase and amplitude of the waveforms. In Sec. IV we calculate the detector mismatch between the waveforms for a range of masses and detectors, and determine the SNR below which the waveforms would be indistinguishable for a single GW detector. In Sec. V we draw some conclusions from our comparisons.

## II. NUMERICAL WAVEFORMS

### A. The physical system

We restrict our attention to the modeling of one physical system, the orbital inspiral of two black holes of *equal mass and zero spin* with vanishing eccentricity. The size of the orbits decreases as the system loses energy through gravitational-radiation emission, until the black holes merge to form a single spinning black hole. The final mass and spin, which determine, for example, the ringdown frequencies, are routinely determined from numerical simulations with a variety of methods; for early results see e.g. [14–16,95,96]. Current simulations are able to obtain very accurate results for the final black-hole parameters, and as examples we quote the results and error estimates reported for the  $\text{SpEC}$  and BAM codes [59,61], which are consistent within the given error estimates: the mass of the final black hole has been found as  $M_f = 0.95162 \pm 0.00002M$  with  $\text{SpEC}$ , and as  $M_f = 0.9514 \pm 0.0016M$  with BAM; the dimensionless spin (Kerr parameter) has been computed as  $S_f/M_f^2 = 0.68646 \pm 0.00004$  with  $\text{SpEC}$  and as  $S_f/M_f^2 = 0.687 \pm 0.002$  with BAM. This corresponds to a dominant ringdown frequency of the  $\ell = m = 2$  mode of  $M\omega = 0.5539 \pm 0.0018$  (conservative BAM estimate) or  $M\omega = 0.5535 \pm 0.00003$  ( $\text{SpEC}$  estimate), using interpolation in tabulated values of ringdown frequencies given in [97].

If we decompose the gravitational-wave signal from this system into spherical harmonics, the ( $\ell = 2, m = \pm 2$ ) modes dominate. The frequency of these two modes (which are related by a  $\pi/2$  phase shift) is very close to twice that of the orbital motion during inspiral, and steadily increases as the black holes approach merger. The amplitude of the signal is a function of the frequency, and also increases. The signal frequency and amplitude peak around merger, and then the amplitude decays exponentially as the merged black hole rings down to a stationary Kerr black hole. For an equal-mass nonspinning binary, we know from numerical simulations that the peak frequency is approximately  $f_{\text{peak}} \approx 16(M_\odot/M)$  kHz. Five orbits before merger, the wave frequency is  $f \approx 1.95(M_\odot/M)$  kHz, and

100 orbits before merger the frequency is  $f \approx 0.38(M_\odot/M)$  kHz, as estimated by post-Newtonian methods.

The most sensitive ground-based detectors currently in operation, LIGO and Virgo, can detect signals from black-hole binary (BH-BH) mergers out to distances of up to several hundred Mpc (depending on the binary's mass and orientation; see e.g. [1,79,98]). Estimated event rates for BH-BH coalescences are on the order of 1 every few years, but with large uncertainties; see e.g. [99–102]. The future Enhanced LIGO [103] and Virgo+ [4] detectors will increase event rates by  $\sim 5$  times, whereas the Advanced LIGO [104] and Advanced Virgo [105] detectors will increase event rates by roughly 3 orders of magnitude as compared with the current detectors.

These detectors are sensitive to frequencies ranging from  $\sim 10$ –40 Hz up to  $\sim 2$  kHz. The merger signal will be in this frequency range for systems with total masses of roughly  $5$ – $250M_\odot$ . The merger will be in the most sensitive part of the detectors' frequency bands for masses around  $50M_\odot$ , and for that case the detectors will also be sensitive to the signal from the last ten orbits before merger. Theoretical estimates of the noise curves for the four detectors we consider, Enhanced LIGO, Advanced LIGO [81], Virgo [81], and Advanced Virgo [105], are shown in Fig. 1 (for Virgo and Advanced LIGO we use approximate analytical formulas as displayed in [79]).

Astrophysical black holes may form binaries through a number of mechanisms [100,106,107]. In general, the black holes will have different masses and will be spinning (high spins may be typical [108–110]), and the orbits will be eccentric. But gravitational-radiation emission reduces the eccentricity, so for typical comparable-mass inspirals the eccentricity is expected to be negligible [111] by the time the binaries have reached the frequencies we have just discussed (for the situation in globular clusters, see, however, [107]). For this reason most analytical and numerical work in modeling gravitational-wave signals has focused

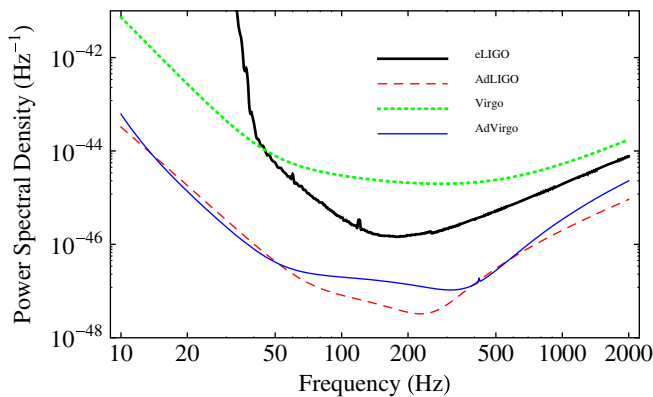


FIG. 1 (color online). Theoretical noise curves [power spectral density  $S_n$ ; see Eq. (12)] for the Enhanced LIGO, Advanced LIGO, Virgo, and Advanced Virgo detectors.

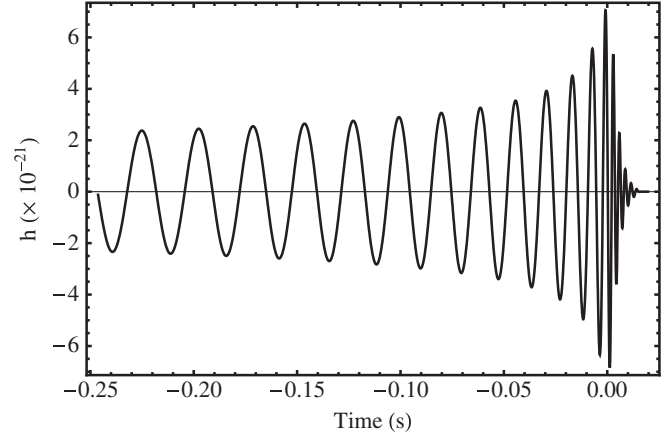


FIG. 2. The gravitational-wave strain from an optimally oriented  $60M_\odot$  equal-mass nonspinning black-hole binary located 100 Mpc away from the detector. The waveform covers about six orbits, or 12 GW cycles, before merger.

on binaries that follow noneccentric (or “quasicircular”) inspiral; see, however, [34,47,64,65] for numerical results on eccentric binaries.

The preceding discussion motivates a focus on the last orbits before merger of binaries following noneccentric inspiral. We study a binary that consists of black holes with equal mass and no spin, simply because this configuration has been studied in the most detail in numerical-relativity simulations. We consider the gravitational-wave signal from the last  $\sim 6$  orbits and merger of this system. Figure 2 shows one polarization of the gravitational-wave strain from an example of such a binary, with total mass  $60M_\odot$ , optimally oriented to the detector and located 100 Mpc away.

## B. Numerical codes

To calculate the gravitational-wave signal in full general relativity, we first require a solution of Einstein's equations. This must be produced numerically, and can be done in a number of different ways. We will compare the results of five computer codes: BAM, CCATIE, Hahndol, MayaKranc, and SpEC. These differ in their procedure for constructing black-hole-binary initial data, decomposition of Einstein's equations into a numerically well-posed and stable form, numerical techniques used to evolve the data, choice of gauge conditions during the evolution, and details of the calculation of the gravitational-wave signal.

We will summarize the different methods of setting up the initial data, the formulations of Einstein's equations, and the numerical techniques. The purpose is not to provide a full exposition of these methods (the full technical details can be found in the references given in Table I) but to make clear the similarities and differences of the five codes.

TABLE I. Summary of numerical codes. The initial separation is the coordinate separation between the punctures (for moving-puncture codes) or between the centers of the excision surfaces (SpEC). The initial momenta specified in the moving-puncture codes are  $(p_t, p_r)/M$ , where  $p_t/M$  is the tangential momentum and  $p_r/M$  is the radial momentum. The SpEC parameters are described in [32]. “Bulk FD order” indicates the spatial finite-difference order in the bulk of the computational domain (i.e., not including mesh-refinement boundary zones).  $h_{\min}$  is the spatial resolution on the finest mesh-refinement level or domain. The wave extraction radii are given, and  $r_{\text{ex}} \rightarrow \infty$  indicates that the results were then extrapolated to infinity. The references provide full details of the implementation of the codes and the simulations that were used in this study. For the CCATIE result, no numerical convergence results were published, but based on the code specification and resolution for this run, a phase accuracy between the Hahndol and BAM/MayaKranc results can be assumed. The amplitude errors quoted for CCATIE and MayaKranc were estimated for the present paper and were previously unpublished.

Code	Initial parameters	Bulk FD order	$h_{\min}/M$ ( $\times 10^{-3}$ )	Wave extraction radius	Eccentricity	Phase uncertainty (radians)		Amplitude uncertainty (percentage)	
						inspiral merger	inspiral merger	inspiral merger	inspiral merger
Finite-difference moving-puncture codes									
BAM [84,85]	$D = 12M$ ; $(0.085, -5.373 \times 10^{-4})$	6	19	$90M$	$e < 0.0016$	0.1	1.0	4.0	6.0
CCATIE [51]	$D = 11M$ ; $(0.090, -7.094 \times 10^{-4})$	4	20	$120M$	$e < 0.0016$			2.0	5.0
Hahndol [25,86,87]	$D = 10.8M$ ; $(0.0912, 0.0)$	4	19	$60M$	$e < 0.008$	2.4	5.0	10.0	10.0
MayaKranc [37]	$D = 12M$ ; $(0.085, -5.343 \times 10^{-4})$	4	15.5	$r_{\text{ex}} \rightarrow \infty$	$e < 0.0016$	0.1	1.1	4.0	8.0
Pseudospectral excision code									
SpEC [31,61]	$D = 14.436M$ ; $r_{\text{exc}} = 0.41360M$ , $M\Omega_0 = 0.016708$ , $v_r = -4.26 \times 10^{-4}$ , $f_r = 0.939561$	n/a	$\sim 3$	$r_{\text{ex}} \rightarrow \infty$	$e < 5 \times 10^{-5}$	0.006	0.02	0.1	0.3

### 1. Initial data

Four of the codes, BAM, CCATIE, MayaKranc, and Hahndol, use Bowen-York puncture initial data [112]. The chief features of these data are that the spatial metric is conformally flat, and the physical momenta and spins of the black holes can be specified directly as parameters in the Bowen-York solution of the momentum constraint [113]. The black holes manifest themselves in the data through topological wormholes, which also allow the spatial slices to bypass the black-hole singularities. The wormholes are compactified so that their ends are mapped to single points, or “punctures” [112,114–117]. The nature of these wormholes changes during a dynamical evolution [91,118–120], but the spatial slices never reach the singularities, and the data can be evolved without recourse to excising any region of the computational domain.

The data used in each code differ only in the choices of initial separation of the black-hole punctures, and their momenta, and in the method of numerically solving the Hamiltonian constraint in the puncture approach; this last distinction will affect the accuracy of the solution of the Hamiltonian constraint, but we assume in this work that the solution used by all four codes is sufficiently accurate that the remaining numerical errors do not contribute to the differences we measure in the final results.

Ideally, the momenta are chosen to produce noneccentric quasicircular inspiral. In the simulation from the Hahndol code, the initial momenta were modified by hand until a roughly quasicircular inspiral was obtained. The BAM, CCATIE, and MayaKranc simulations used parameters calculated by post-Newtonian methods, as out-

lined in [56]. This procedure results in an eccentricity of  $e < 0.0016$ . The choices of initial momenta are given in Table I.

The SpEC code uses excision data: the data extend only to the black-hole apparent horizons. The data were constructed by solving the conformal-thin-sandwich initial-value equations [121,122], with suitable boundary conditions on the apparent horizons and at the outer boundary to produce nonspinning black holes [123–125] in an orbit with small radial velocity [32]. The parameters appropriate to quasicircular inspiral were first predicted by the methods described in [125], and then modified using the iterative procedure described in [31,32], to yield an eccentricity of below  $e \sim 5 \times 10^{-5}$ . Once again the data are conformally flat.

The reader should not make too much (or too little) of the differences between these two types of data, Bowen-York-puncture and conformal-thin-sandwich-excision. Although they are constructed in quite different ways, both sets of data are based on similar choices of the free data in initial-value equations (in particular, conformal flatness), and may not be physically very different; elucidating their exact differences is not trivial. Conversely, they are not identical, and there is no reason to expect *a priori* that the waveforms resulting from evolutions of both sets of data will precisely agree. Evaluating that difference is part of the analysis in this work.

### 2. Evolution systems

The codes that start with puncture initial data—BAM, CCATIE, MayaKranc, and Hahndol—evolve the data



with the BSSN formulation of Einstein’s equations, and follow [15,16] in the use of coordinate conditions that allow the black holes to move across the grid. The BSSN evolution system [88–90] is combined with hyperbolic evolution equations for the lapse and shift (1 + log slicing [126] and the  $\tilde{\Gamma}$ -driver shift condition [87,90]), which have been shown to lead to a well-posed initial-value problem [92].

The `SpEC` code uses a first-order formulation [94] of the generalized-harmonic-gauge system [93,127] with built-in constraint-damping terms [128,129]. This system is manifestly symmetric hyperbolic and well posed. The gauge source functions are chosen to be constant in a comoving frame during the inspiral [22], and are evolved according to a sourced wave equation during merger and ringdown [61]. The characteristic fields of the system are all outward flowing (into the holes) at the excision boundaries, so no boundary conditions are needed or imposed there. The outer boundary conditions [94,130,131] are designed to prevent the influx of constraint violations [132–138] and undesired incoming gravitational radiation [139], while allowing the outgoing gravitational radiation to pass through the boundary.

### 3. Numerical techniques

The moving-puncture codes solve the partial-differential equations of the BSSN formulation of the Einstein equations with finite-difference methods. The numerical domain consists of nested Cartesian domains, such that successive levels of refinement are placed both around the individual black holes (and centered on the punctures) and around the entire black-hole-binary system (centered on the origin of coordinates). The details of the mesh refinement differ between codes, and the full details can be found in the relevant references. The spatial finite differencing is, in general, fourth order in `Hahndol`, `CCATIE`, and `MayaKranc`, and sixth order in `BAM`. Here, centered differences are used with the exception of shift advection terms, which use one-point lopsided stencils. Integration forward in time is performed with a fourth-order Runge-Kutta method. The `Hahndol` code uses a uniform time step, while the other BSSN codes use variants of a Berger-Oliger scheme, where finer grids can evolve with smaller time steps. The refinement boxes that are centered around the black holes move with them through the grid.

The `SpEC` code uses multidomain pseudospectral methods on a grid with two excised regions, one just inside the apparent horizon of each hole, and employs a dual-frame technique to track the motion of the holes [22]. The computational domain consists of two sets of concentric spherical shells (one surrounding each excised region), another set of concentric spherical shells extending to the outer boundary, and a structure of touching cylinders that fills in the remaining volume and overlaps some of the spherical shells. Interdomain boundary conditions are enforced with

a penalty method [140,141]. Time stepping is accomplished via the method of lines, using an adaptive fourth/fifth-order Runge-Kutta method.

### 4. Summary of the numerical codes and waveforms

Table I summarizes the similarities and differences of the five waveforms, and the codes used to produce them. More details on the waveforms can be found in the following references: The `BAM` waveform is from the highest-resolution D12 simulation described in [55]. The `CCATIE` results have been obtained from the simulation described in [49]. The `MayaKranc` simulation is the  $e = 0$  simulation described in [34]. The `SpEC` waveform corresponds to the waveform “30c-1/N6” described in Ref. [61]; the inspiral portion of this waveform is more comprehensively discussed in Ref. [31], including a detailed error analysis. The `Hahndol` waveform comes from the highest-resolution (grid spacing of  $M/32$  at the finest level) evolution of the “ $d_i = 10.8 M$ ” data presented in [24]. The `BAM`, `CCATIE`, `Hahndol`, and `MayaKranc` simulations employed a nominal Courant factor of 0.5, although for the `BAM`, `CCATIE`, and `MayaKranc` simulations the Courant factor was lowered on the two outermost mesh-refinement levels. `SpEC` used adaptive step-size control, which resulted in time steps close to the Courant instability limit.

No new simulations were performed for this paper, although the `MayaKranc` waveform results from an updated extrapolation procedure as described in Sec. II C.

Table I also provides uncertainty estimates in the GW phase and amplitude, quoted separately for the inspiral regime (up to a frequency of roughly  $M\omega = 0.2$ ), and the merger and ringdown regime. It is important to bear in mind that each uncertainty estimate applies only to the *waveform*, and not to the *code* used to produce it. For example, a code that uses second-order-accurate finite differencing may well produce waveforms that are more accurate than any presented here, if run at sufficiently high resolution with sufficiently accurate initial data, and if the gravitational waveforms were extracted sufficiently far from the source.

Note that the apparent accuracy of the phase and amplitude depend strongly on how one chooses to align waveforms from different simulations, and whether quantities are considered as functions of time, phase, or frequency. All of these choices are valid when comparing results produced by evolving the same initial data with the same evolution system, and varying only numerical resolution, radiation extraction radii, and outer boundary location, and one is free to make the choice that gives the lowest error estimate. As such, the methods used to estimate the phase and amplitude errors differ for each waveform; more details can be found in some of the references listed in Table I.

Having said that, in the present study we are comparing results from different codes, with different initial data and

gauge conditions, and the disagreements we see from different waveform alignment choices may exaggerate, or hide, the “real” differences between the waveforms.

We find that the least ambiguous method of comparison is to plot quantities with respect to the frequency  $M\omega$  of the  $(\ell = 2, m = 2)$  mode of  $\Psi_4$ . This choice removes the need to apply a time and phase shift when comparing the wave amplitude, and the freedom of a constant phase shift in a phase comparison is straightforward to interpret.

### C. Extraction of gravitational waves

In the numerical simulations presented here, the gravitational waves are extracted using the Newman-Penrose Weyl tensor component  $\Psi_4$  [142,143], which, at infinite separation from the source, is related to the complex strain  $\mathbf{h} = h_+ - ih_\times$  by [144]

$$\mathbf{h} = \lim_{r \rightarrow \infty} \int_0^t dt' \int_0^{t'} dt'' \Psi_4. \quad (1)$$

Note that the amplitude of the gravitational-wave strain falls off as  $1/r$ , where  $r$  is the distance of the detector (or, in a numerical code, the extraction sphere) to the source, and so we generally consider  $r\mathbf{h}$  (and  $r\Psi_4$ ), which in the weak-field region will be independent of  $r$ .

It is useful to discuss gravitational-radiation fields in terms of spherical harmonics of spin-weight  $s = -2$ ,  $Y_{\ell m}^s$ , which represent symmetric tracefree two-tensors on a sphere, and in this paper we will only consider the dominant  $\ell = 2, m = \pm 2$  modes, with basis functions

$$Y_{2-2}^{-2} \equiv \sqrt{\frac{5}{64\pi}} (1 - \cos\theta)^2 e^{-2i\varphi}, \quad (2)$$

$$Y_{22}^{-2} \equiv \sqrt{\frac{5}{64\pi}} (1 + \cos\theta)^2 e^{2i\varphi},$$

i.e., we will consider the cases  $\ell = 2, m = \pm 2$  of the projections

$$\mathbf{h}_{\ell m} \equiv \langle Y_{\ell m}^{-2}, \mathbf{h} \rangle = \int_0^{2\pi} d\varphi \int_0^\pi \mathbf{h} \bar{Y}_{\ell m}^{-2} \sin\theta d\theta, \quad (3)$$

of the complex strain  $\mathbf{h}$  (the bar denotes complex conjugation). In the nonspinning case considered here, we have equatorial symmetry so that  $\mathbf{h}_{22} = \bar{\mathbf{h}}_{2-2}$ , and

$$\mathbf{h}(t) = \sqrt{\frac{5}{64\pi}} e^{2i\phi} ((1 + \cos\theta)^2 \mathbf{h}_{22}(t) + (1 - \cos\theta)^2 \bar{\mathbf{h}}_{22}(t)).$$

The coordinate radius at which the waves were extracted from the numerical solution is given for each code in Table I. For the *MayaKraNC* and *SpEC* codes, the waves were extracted at several radii, and then extrapolated to  $r_{\text{ex}} \rightarrow \infty$ , to give a more accurate estimate of the wave that would be measured by a distant GW detector. The extrapolation procedure involves aligning the waveforms with respect to some definition of retarded time [31], and then

treating the error due to the extraction radius as a polynomial in powers of  $1/r_{\text{ex}}$  [31,55]. Different polynomial fits were performed for the inspiral and merger for the *MayaKraNC* waveform, and the specific extrapolation procedure used for the *SpEC* waveform is given in [31,61]. Waves were extracted from the *CCATIE* simulation using the Zerilli-Moncrief procedure (see [145] for a review), from which  $\Psi_4$  can be readily derived.

The direct waveform comparisons in Sec. III deal with  $r\Psi_4$ . The data-analysis comparisons in Sec. IV are based on the strain,  $r\mathbf{h}$ . To produce the strain from  $\Psi_4$  one needs “merely” to integrate twice with respect to time, as in Eq. (1), and choose appropriate integration constants. However, this procedure is not as trivial as it appears at first. One might naively assume that integration constants could be chosen on simple physical grounds, for example, that the strain rings down to zero after the black holes have merged, and that it oscillates around zero at all times. Such requirements have been found to work adequately in some cases for the  $(\ell = 2, m = 2)$  mode, but even in the best cases unusual artifacts remain, and these become more pronounced when one considers higher modes; see [146] for some examples. One reason for these difficulties is that the waveforms contain small numerical errors and gauge effects, which become greatly exaggerated when integrated over the entire duration of the waveform—and to calculate the strain we must perform such an integration twice.

A tempting alternative is to work only in the Fourier domain. Start with the numerically generated  $\Psi_4(t)$  and calculate the Fourier transform  $\tilde{\Psi}_4(f)$ ; then it is trivial to perform two time integrations to obtain the Fourier transform of the strain,

$$\tilde{\mathbf{h}}(f) = -\frac{\tilde{\Psi}_4(f)}{4\pi^2 f^2}. \quad (4)$$

The integration constants have been ignored in this procedure, or, rather, they have been implicitly set to zero. If we now perform an inverse Fourier transform to calculate  $\mathbf{h}(t)$ , we will recover artifacts similar to those we would have seen if we had performed two time integrations of  $\Psi_4(t)$ .

However, in this paper we use this very method to calculate  $\tilde{\mathbf{h}}(f)$  to use in our match calculations. Our justification is that, for a selection of waveforms, we have independently calculated  $\mathbf{h}(t)$  by a number of different methods (with varying levels of success in removing numerical and gauge artifacts in the final strain), and have then used the Fourier transform of this quantity in match calculations and obtained very similar results; we will discuss the impact of the small differences that we see in Sec. IV. Our conclusion is that the choice of integration constants, and modifications that “clean” the waveform of nonphysical artifacts, although they may lead to serious differences in the time-domain waveform, do not signifi-

cantly affect the match calculation for the ( $\ell = 2, m = 2$ ) mode.

### III. DIRECT COMPARISON OF PHASE AND AMPLITUDE

We now compare the waveforms produced by the five codes. For the purposes of gravitational-wave detection, the most meaningful comparison will include the noise spectrum of the detector. We will make comparisons relevant to detection and parameter estimation in Sec. IV. In this section we directly compare the numerical waveforms in a manner that is independent of any particular detector. The quantities we will compare are the amplitude  $A(t)$  and the phase  $\phi(t)$  of the ( $\ell = 2, m = 2$ ) mode of  $r\Psi_4$ , which are defined by

$$r\Psi_{4,22}(t) = A(t)e^{-i\phi(t)}. \quad (5)$$

The GW frequency for the ( $\ell = 2, m = 2$ ) mode is given by  $\omega(t) = \dot{\phi}(t)$ .

The amplitude and phase are the two pieces of raw output from the computer code that define the waveform, so they allow the most direct comparison between results from different codes. More generally, an amplitude/phase comparison allows us to quantify waveform differences independent of any detector—if two waveforms accumulate one cycle of phase disagreement during the last ten cycles before they reach the peak amplitude, that is a difference that will exist no matter which detector they pass through.

On the other hand, there are a number of ambiguities in an amplitude/phase comparison, which we will describe as we proceed. For the purpose of gravitational-wave detection, the detector mismatch and SNR are more meaningful quantities to compare. We can summarize the situation as follows: a direct comparison of amplitude and phase is most useful to the numerical relativist, while the mismatch and SNR are most useful to the data analyst.

#### A. Phase

In comparing the phases of two waveforms from different simulations,  $\phi_1(t_1)$  and  $\phi_2(t_2)$ , we cannot simply calculate  $\phi_1(t_1) - \phi_2(t_2)$ , because the time coordinates  $t_1$  and

$t_2$  may not be the same. The two simulations may have been started at different points along the binary inspiral, meaning that  $t_1 = 0$  does not label the same event as  $t_2 = 0$ . More simply, although the waveforms may be identical, one will reach a detector later than the other.

To make a comparison, we first have to decide on an event at which the two waveforms should agree, and then apply a relative time shift and phase shift so that the chosen event occurs at the same time and phase for each waveform. For example, if we were to align the phases at the time when the waveform amplitude reaches a maximum, then we would first determine the times  $T_1$  and  $T_2$  when each waveform's amplitude reaches its maximum, and then study the quantity

$$\Delta\phi(t) = \phi_1(t + T_1) - \phi_2(t + T_2) + \phi(T_2) - \phi(T_1), \quad (6)$$

where, by construction, the amplitude maxima now occur at  $t = 0$  and  $\Delta\phi(0) = 0$ .

The problem with this procedure is that  $\Delta\phi(t)$  is extremely sensitive to the accuracy with which  $T_1$  and  $T_2$  were determined, particularly around the merger, when the GW frequency increases rapidly. One solution is to make a further small time shift, until the overall phase disagreement between the two waveforms has been minimized. Such a suggestion has been used in the past in matching NR and PN waveforms [78,147], and in NR-PN comparisons [62]. This, however, is an approach designed not to determine the differences between two waveforms, but to minimize them. Another option, which avoids the time-shift ambiguity altogether, is to compare the phases as a function of GW frequency  $\phi(M\omega)$ ; this procedure was used in [25], and we will use it here.

The GW frequency as read from the numerical data is too noisy at early and late times to allow a clean direct parametric plotting of phase vs frequency. We instead fit the frequency to a combination of the TaylorT3 PN frequency formula [148] and a modification of the frequency ansatz introduced in [68]. Specifically, the TaylorT3 expression for the orbital frequency of the binary during inspiral is given up to 3.5PN order by [148,149]

$$\begin{aligned} \Omega_{\text{PN}}(\tau) = & \frac{1}{8}\tau^{-3/8} \left[ 1 + \left( \frac{743}{2688} + \frac{11}{32}\nu \right) \tau^{-1/4} - \frac{3}{10}\pi\tau^{-3/8} + \left( \frac{1855099}{14450688} + \frac{56975}{258048}\nu + \frac{371}{2048}\nu^2 \right) \tau^{-1/2} \right. \\ & + \left( -\frac{7729}{21504} + \frac{13}{256}\nu \right) \pi\tau^{-5/8} + \left( -\frac{720817631400877}{288412611379200} + \frac{53}{200}\pi^2 + \frac{107}{280}\gamma - \frac{107}{2240}\ln\left(\frac{\tau}{256}\right) \right. \\ & \left. \left. + \left( \frac{25302017977}{4161798144} - \frac{451}{2048}\pi^2 \right) \nu - \frac{30913}{1835008}\nu^2 + \frac{235925}{1769472}\nu^3 \right) \tau^{-3/4} + a(\nu)\tau^{-7/8} \right], \quad (7) \end{aligned}$$

where we have given the last (3.5PN) term an arbitrary coefficient,  $a(\nu)$ , where  $\nu$  is the symmetric mass ratio  $\nu = m_1 m_2 / M^2$ . This term is known in PN theory, but we will

instead fit it to our numerical data, given our modified definition of the variable  $\tau$ , which we will now discuss. The definition of  $\tau$  in standard PN theory is

$$\tau = \frac{\nu(t_c - t)}{5M}, \quad (8)$$

where  $t_c$  is a PN estimate of the ‘‘coalescence time.’’ The expression (7) diverges when  $\tau = 0$ , so in order to produce a formula through which our data fit, we use instead

$$\tau^2 = \frac{\nu^2(t_c - t)^2}{25M^2} + 1, \quad (9)$$

and we now treat  $t_c$  as a parameter to fit to the data, as in [148]. With our new definition of  $\tau$ , the expression (7) becomes inaccurate near  $\tau = 0$  (which is true anyway for any post-Newtonian expression near merger), but does not diverge. To model the ringdown phase, we modify the ansatz suggested in [68], and write the full frequency as

$$\begin{aligned} \Omega(t) &= \Omega_{\text{PN}}(\tau) + (\Omega_f - \Omega_{\text{PN}}(\tau)) \\ &\times \left( \frac{1 + \tanh[\ln\sqrt{\kappa} - (t - t_0)/b]}{2} \right)^\kappa. \end{aligned} \quad (10)$$

The constants  $\{t_c, t_0, \kappa, a, b, \Omega_f\}$  are parameters that are determined to produce the best fit to the numerical data. The constant  $\Omega_f$  corresponds to a fit of the ringdown frequency. The frequency as a function of time is shown for the BAM code in Fig. 3, as calculated from the raw numerical data, and as given by the fitting procedure we have just described; the GW frequency is related to the orbital frequency by a factor of 2. The GW phase as a function of frequency for each of the five waveforms is shown in Fig. 4.

Figure 5 compares the phase of each waveform with that from the SpEC code. The GW frequency 1000*M* before merger, where our waveforms nominally begin, is close to  $M\omega = 0.055$ , and this is the frequency at which our comparison begins. After merger, the merged black hole rings down to the Kerr solution, and the GWs are emitted at the ringdown frequency, which is close to  $M\omega = 0.55$ ; this is

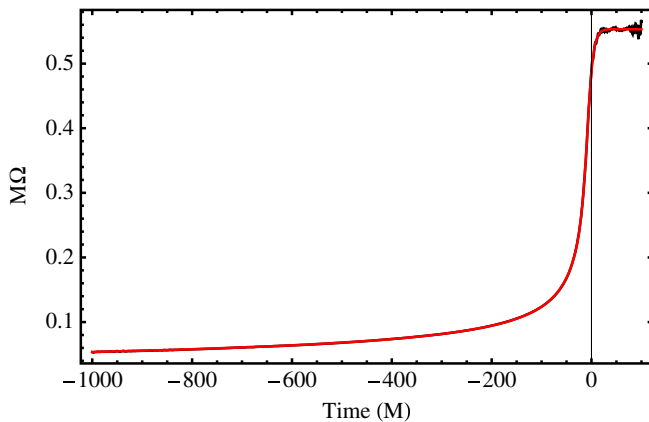


FIG. 3 (color online). The GW frequency as calculated from the raw BAM data, and as given by the fitting procedure described in the text. The two lines are indistinguishable if viewed in black-and-white.

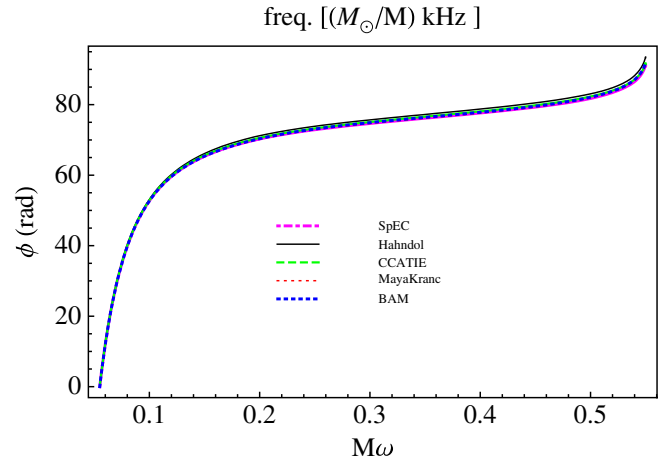


FIG. 4 (color online). GW phase  $\phi$  as a function of frequency  $M\omega$ , for the five codes. The frequency is given both in terms of the dimensionless orbital frequency  $M\omega$  and the frequency in kHz scaled with respect to the total mass of the binary in solar masses.

where we end our comparison. (The precise ringdown frequency for the equal-mass, nonspinning, zero-eccentricity configuration is  $M\omega = 0.5535$  [61].)

In the left panel of Fig. 5 we show the phase disagreement during inspiral, ending at  $M\omega = 0.2$ , which is reached about half an orbit before merger. A phase shift is applied so that the phases all agree at  $M\omega = 0.055$ . We see that the accumulated phase disagreement is below 0.3 radians for all codes except Hahndol, for which the larger eccentricity and lower resolution lead to larger dephasing against the SpEC results. The behavior of the three other waveforms is roughly consistent with the numerical methods used to produce them: the BAM waveform was produced with the highest-order spatial finite differencing (sixth order), and while fourth-order spatial finite differencing was used to produce both the CCATIE and MayaKranc results, the MayaKranc simulation was performed at slightly higher resolution, and the results were further extrapolated with respect to the radiation extraction radius.

The most important point is that the results of each code agree within their respective uncertainty estimates.

The right panel of Fig. 5 shows the accumulated phase disagreement during the last orbit, merger, and ringdown. The phases are shifted to agree at the lowest frequency shown in the figure,  $M\omega = 0.2$ , so that we can see how the phase disagreement behaves during the merger regime only. Note that the waveform from the Hahndol simulation becomes very noisy late in the ringdown, which accounts for the poor behavior above  $M\omega \approx 0.52$ . Note also that while the merger and ringdown plot sweeps through roughly twice the range of frequencies as the inspiral plot, the length of time covered during the inspiral (about 900*M*) is much *greater* than that during the merger (about 180*M*).



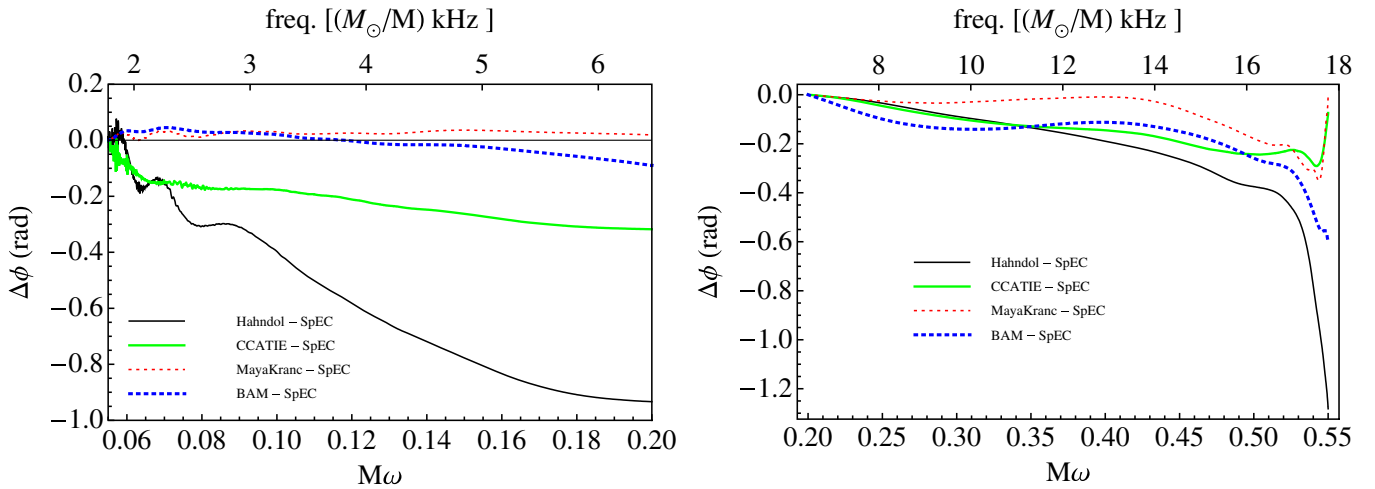


FIG. 5 (color online). Phase comparison. The left panel shows the phase comparison between the SpEC waveform and the others during inspiral, from  $M\omega = 0.055$  up to  $M\omega = 0.2$ , which is about one orbit before merger. The corresponding uncertainty estimates are 0.1 rad (BAM and MayaKranc) and 2.4 rad (Hahndol). The right panel shows the phase comparison during merger and ringdown, from  $M\omega = 0.2$  up to  $M\omega = 0.55$ . The uncertainty estimates during merger are, in radians, 1.0 (BAM), 1.1 (MayaKranc), and 5.0 (Hahndol). In both panels a phase shift was applied so that the phases agreed at the lowest frequency shown.

In this sense the phase disagreement grows more quickly during merger. The phase disagreements of the different waveforms are again consistent with uncertainty estimates, but are larger for merger and ringdown than they were during inspiral.

The two panels of Fig. 5 were designed to show separately the phase difference accumulated during inspiral, or during merger/ringdown. When considering the phase as a function of frequency (as done in Fig. 5), the only freedom is an overall additive constant to the phase. Thus, the total accumulated phase difference during inspiral *and* merger/ringdown can be obtained by vertically offsetting the curves in the right panel of Fig. 5, so that the phase differences at  $M\omega = 0.2$  agree in both panels. For instance, the total accumulated phase difference between BAM and SpEC at  $M\omega = 0.52$  would be the sum of 0.1 rad (from the left panel of Fig. 5) and 0.28 rad (from the right panel), i.e., 0.38 rad. For the other codes, one finds at  $M\omega = 0.52$  the following total accumulated phase differences relative to SpEC: Hahndol 1.36 rad, CCATIE 0.55 rad, and MayaKranc 0.18 rad. The reader may choose to calculate the total accumulated phase disagreement at any frequency, although one should bear in mind that beyond  $M\omega = 0.52$  the curves in Fig. 5 are less reliable, due to errors in the curve fit equation (10) through noisy numerical data.

## B. Amplitude

In comparing the GW amplitude between codes, we once again consider the amplitude as a function of frequency,  $A(M\omega)$ , which is shown for the five codes in Fig. 6. The amplitude comparison is shown in Fig. 7. Once again, the comparison during inspiral, shown in the left panel,

covers the frequency range  $M\omega \in [0.055, 0.2]$ , and the comparison during merger and ringdown, shown in the right panel, covers the frequency range  $M\omega \in [0.2, 0.55]$ . The oscillations in the right panel of Fig. 7 are probably due to small errors from gauge effects that are exaggerated in this plot by the rapid change in the GW frequency near merger. Recall that the Hahndol waveform becomes unreliable at about  $M\omega \approx 0.52$ .

Note once again that the agreement is within the estimated uncertainties of the waveforms.

The conclusion of our direct comparison of the GW phase and amplitude is that all five codes are consistent within their stated error bars. This provides an important consistency check on the numerical accuracy and validity

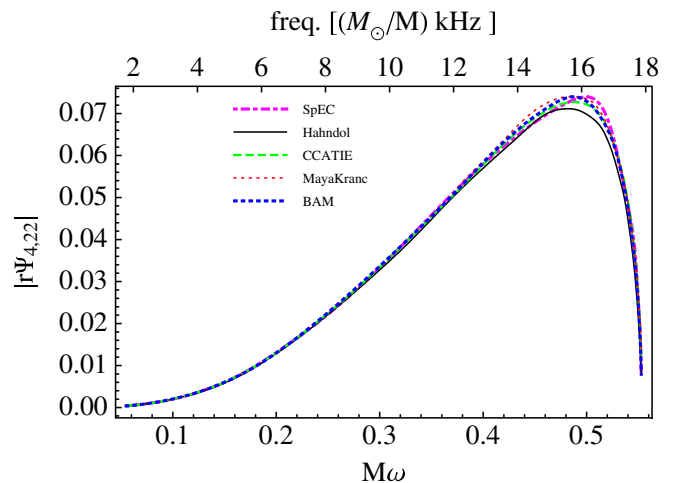


FIG. 6 (color online). The amplitude as a function of GW frequency,  $A(\omega) = |r\Psi_{4,22}|$ , for the five codes.

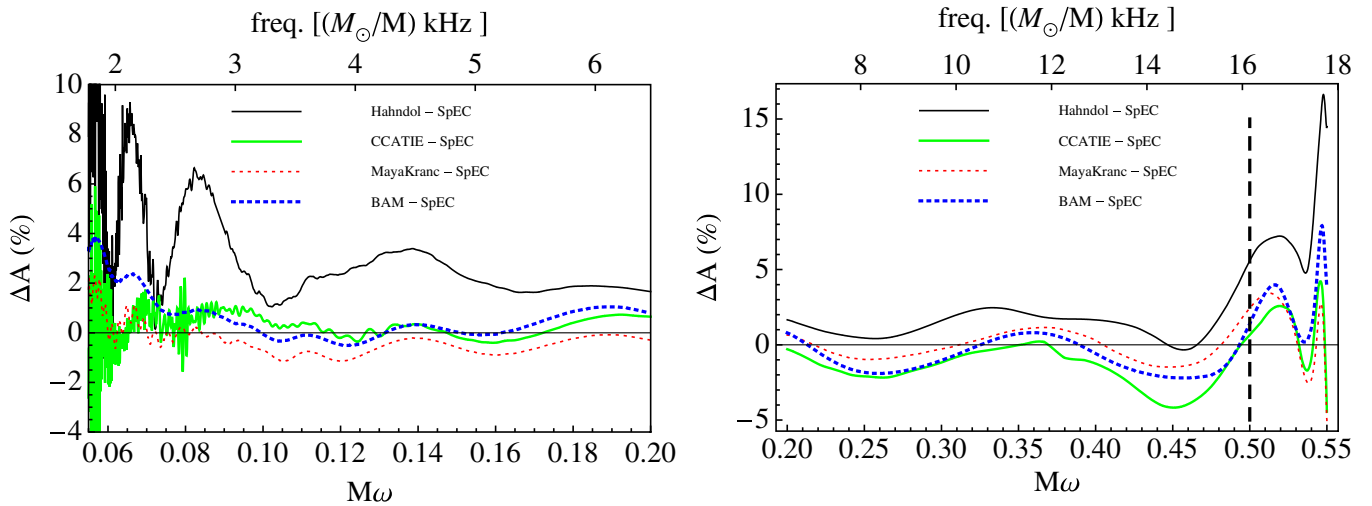


FIG. 7 (color online). Comparison of the amplitude as a function of GW frequency,  $A(\omega)$ . The left panel shows the percentage disagreement during inspiral (up to  $M\omega = 0.2$ ). The corresponding amplitude uncertainties are 2% (CCATIE), 4% (BAM and MayaKranc), and 10% (Hahndol). The right panel shows the same quantity during merger and ringdown, for which the uncertainties are 5% (CCATIE), 6% (BAM), 8% (MayaKranc), and 10% (Hahndol). The vertical dashed line indicates the approximate location of the amplitude maximum,  $M\omega = 0.5$ .

of each waveform. Not only that, it provides us with an upper limit on the variations in the waveforms due to different choices of initial data (in these cases puncture data versus quasiequilibrium conformal-thin-sandwich excision data), and different gauge choices. The latter can lead to noticeable differences in the amplitude and phase of the waveform extracted from the simulation (see, for example, the discussions in [61,84,150]). With suitable gauge choices these differences should decrease as the waves are extracted successively further from the source, and indeed it is usually possible to perform some procedure to extrapolate the waveform to estimate the result that would be measured infinitely far away [31,55,61,65]. These are delicate procedures, and one may still worry that the different gauge choices between codes will lead to large differences in the final waveforms. In this section we have shown that, if such differences exist, they are small and within the error bars of each simulation.

The results so far provide information that allow numerical relativists to quantify the accuracy and consistency of their results. In the next section we will make comparisons relevant to data analysis and GW astronomy.

#### IV. DETECTION

A more meaningful comparison from the point of view of GW *detection* is the best match (and mismatch) between waveforms [151].

The match is usually calculated in the frequency domain. Consider two time series  $x(t)$  and  $y(t)$ , which will be the two waveforms we wish to compare. The Fourier transform is given by

$$\tilde{x}(f) = \int_{-\infty}^{\infty} x(t)e^{2\pi ift} dt. \quad (11)$$

(In LSC applications the opposite sign convention is used for the phase in the Fourier transform definition, but the choice of sign does not affect the results here.) In practice, we calculate a discrete Fourier transform on the numerical data. We calculate the time when the wave amplitude reaches its maximum,  $t_{\max}$ , and then truncate the waveform  $1000M$  before this time, and  $80M$  after. The resulting truncated waveform is then resampled every  $0.1M$ , to give a data set with 10 800 points. We then take a discrete Fourier transform of each such data set, and retain only the half of the data set that covers positive frequencies. We also verified that our results did not change significantly when the sampling rate was increased.

We can define an inner product between  $\tilde{x}(f)$  and  $\tilde{y}(f)$  weighted with the noise spectrum of the detector,  $S_n(f)$  [152],

$$\langle x|y \rangle := 4 \operatorname{Re} \left[ \int_{f_{\min}}^{f_{\max}} \frac{\tilde{x}(f)\tilde{y}^*(f)}{S_n(f)} df \right]. \quad (12)$$

In the same way we define a norm of a waveform  $\tilde{x}(f)$  by  $|x| = \sqrt{\langle x|x \rangle}$ .

The SNR is defined with respect to this waveform norm. Recall that throughout this paper we have been dealing with  $r\mathbf{h}$  and  $r\Psi_4$ , where  $r$  is the distance of the detector (or numerical wave extraction) from the source, and one should remember to use the real strain  $\mathbf{h}$  in the definition of the SNR. For clarity, let us define  $\tilde{\mathbf{h}} = r\mathbf{h}$ , as calculated from the numerical code, and then the SNR is given by

$$\rho = \frac{\sqrt{\langle \tilde{h} | \tilde{h} \rangle}}{R}, \quad (13)$$

where  $R$  is the distance of the source from the detector, usually in units of Mpc.

The best match [151] is defined as the inner product  $\langle x|y \rangle$  normalized by the norms of each waveform, and maximized over relative time and phase shifts ( $\tau$  and  $\Phi$ ) between the two waveforms:

$$\mathcal{M} = \max_{\tau, \Phi} \frac{\langle x|y \rangle}{\sqrt{\langle x|x \rangle \langle y|y \rangle}}. \quad (14)$$

We can view this procedure as adjusting the waveforms with respect to their time of arrival, and their initial phase, such that we achieve the best agreement.

One convenient way [153] to calculate the best match with respect to the phase shift is to first normalize each polarization of the two waveforms as  $e_{1+,x} = \tilde{x}_{+,x}/|x_{+,x}|$  and  $e_{2+,x} = \tilde{y}_{+,x}/|y_{+,x}|$ , and to define

$$\begin{aligned} A &= \langle e_{1+}|e_{2+} \rangle^2 + \langle e_{1+}|e_{2\times} \rangle^2, \\ B &= \langle e_{1\times}|e_{2+} \rangle^2 + \langle e_{1\times}|e_{2\times} \rangle^2, \\ C &= \langle e_{1+}|e_{2+} \rangle \langle e_{1\times}|e_{2+} \rangle + \langle e_{1+}|e_{2\times} \rangle \langle e_{1\times}|e_{2\times} \rangle. \end{aligned}$$

In general, one should also orthonormalize the two waveforms, but in this work we consider only optimally oriented binaries, and so this is not necessary. The best match is then given by [153]

$$\mathcal{M} = \max_{\tau} \left[ \frac{A+B}{2} - \left[ \left( \frac{A-B}{2} \right)^2 + C^2 \right]^{1/2} \right]^{1/2}. \quad (15)$$

For the waveforms we consider here, the match is very close to unity, and it makes more sense to quote the mismatch, defined as  $1 - \mathcal{M}$ .

In evaluating (12), we must choose  $f_{\min}$  and  $f_{\max}$ . Ideally these would be  $(0, \infty)$ , but in practice they are based on the range of frequencies for which the Fourier transform is reliable (very high and very low frequencies contain unphysical artifacts due to numerical errors and the sampling rate of the data), and the relevant frequency window of a given detector. The frequency range for the Enhanced LIGO detector is chosen as 30 Hz up to 2 kHz, and for the Advanced LIGO, Virgo, and Advanced Virgo detectors it is from 10 Hz up to 2 kHz. The acceptable frequency range for the Fourier transforms of the numerical data is from  $fM = 0.001$  up to  $fM = 1$ . The actual integrals are performed over the intersection of the detector and waveform frequency ranges.

The time shift  $\tau$  deserves some discussion. From our experience with phase comparisons in Sec. III we know that, in general, we must time shift two waveforms with respect to each other in order to realistically estimate their agreement. It is natural to apply that time shift to one of the waveforms in the time domain, but if we have the entire frequency-domain representation of the signal, we can also

calculate the effect of a time shift on the match in the frequency domain. In our case we do *not* have the entire frequency-domain waveform: the numerical waveform was truncated  $1000M$  before merger, and  $80M$  after merger, and as such, the calculated Fourier power is incorrect outside a certain range of frequencies. Put another way, a time shift in the time domain would result in using in our analysis a different  $1080M$ -long portion of one of the waveforms, and there is no way that the analysis of the Fourier transform of one  $1080M$ -long segment of the waveform can capture the effect of choosing a different  $1080M$ -long segment. As such, we apply a time shift to one of the waveforms *before* calculating its Fourier transform, and maximize the match with respect to this time shift.

Figure 8 shows the minimum mismatch between the  $\text{SpEC}$  waveform and each of the other four, for the Enhanced LIGO, Advanced LIGO, Virgo, and Advanced Virgo noise curves. A mass range of  $60\text{--}300M_{\odot}$  was used for the Enhanced LIGO detector, and  $180\text{--}300M_{\odot}$  for the others. The lower mass was dictated by the desire that the waveform begin below the low-frequency cutoff of the detector. At yet lower masses we would need to use longer waveforms, i.e., waveforms that extend to lower frequencies. We can see from these results that the mismatches are excellent: the mismatch is below  $10^{-3}$  in all cases, and for all except the `Hahndol` waveform, it is below  $4 \times 10^{-4}$ . The performance of each waveform is consistent with the expected accuracy of each code, and with the results presented in Sec. III. Recall also that the mismatch calculation usually involves adjusting the mass associated with one of the waveforms, in order to improve the result. If such a minimization (or, in terms of the match, a maximization) were performed here, the mismatches would improve further.

The mismatch is, in general, very sensitive to phase differences, and this may explain the worse mismatch of the `Hahndol` waveform, which shows large variations in the phase disagreement, due mostly to higher eccentricity and lower numerical resolution (see Fig. 5, where the larger dephasing due to eccentricity is apparent). We should note, however, that the mismatch is still extremely small, and easily meets the standard detection criteria, which we will discuss below.

As we pointed out in Sec. II C, the Fourier transform of the strain used for match calculations was produced from the Fourier transform of  $\Psi_4$ ; i.e., we calculated  $\Psi_4(t) \rightarrow \tilde{\Psi}_4(f) \rightarrow \tilde{h}(f)$ . The matches we calculate are very close to unity, and we wish to know how much the results vary if we first calculate the strain  $h(t)$  in the time domain, or if we slightly vary the length of the waveforms in either time or frequency. We tested the robustness of some of our match calculations to these changes, and found that the results could vary by as much as  $2 \times 10^{-4}$ , but the values shown in Fig. 8 were almost always lower than those calculated by other methods. As such, we consider the curves in Fig. 8 as

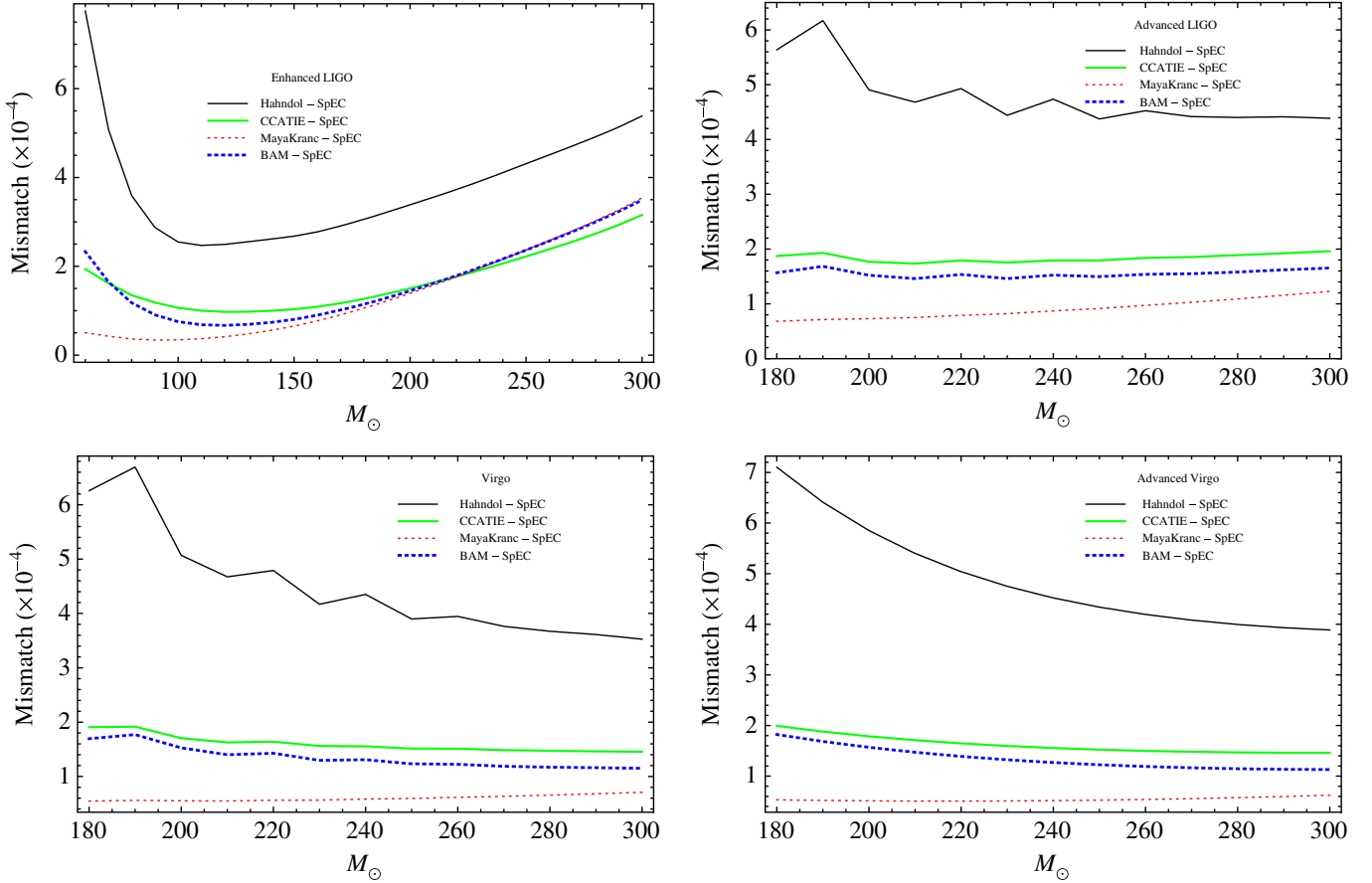


FIG. 8 (color online). The mismatch between the  $\text{SpEC}$  waveform and each of the other codes (the line colors match those in previous plots). The three plots show the results for the Enhanced LIGO, Advanced LIGO, Virgo, and Advanced Virgo noise curves. The lower end of the mass range was chosen such that the entire numerical waveform was included in the detector’s frequency band.

lower bounds on the mismatch, and note that we expect that, in the worst case, they would be no more than  $2 \times 10^{-4}$  higher.

The best mismatch required for detection is usually given as 0.035 [98,154–156], for which no more than 10% of signals will be lost [151]. This is the best mismatch required between a member of a waveform template bank and the true physical waveform that is detected. In LIGO detector searches, templates are constructed such that the worst mismatch between successive members of the template bank is 0.03 [98,154,155]. This places the more stringent requirement on the accuracy of the theoretical waveform of a mismatch better than 0.005; see the discussion in [157]. This threshold is well above the largest mismatches calculated here. The conclusion, then, is that current numerical waveforms are sufficiently accurate for detection purposes with all current and planned ground-based detectors.

### A. Parameter estimation

We now evaluate the differences between the waveforms with respect to the measurement of the source’s param-

eters. The theory of parameter estimation accuracy is developed and discussed in [152,158–160]. We defer a detailed analysis of these waveforms with respect to parameter estimation to future work, and here make a first analysis based on the criterion proposed in [157].

Imagine that a GW signal is detected, and the waveforms studied here are used to estimate the parameters of the source. Each of our numerical waveforms is slightly different, and if the detected signal were strong enough (i.e., the SNR were large enough), the estimated parameters of the source would be different depending on which numerical waveform we used. However, if the SNR is below a certain value, any two of our waveforms will be indistinguishable. To put this discussion in context, a reliable detection requires a SNR above a threshold which is usually chosen between about 5 and 8, depending on details of the detector and search performed (compare e.g. [98,161,162]). Therefore, if the SNR has to be below this threshold value for two waveforms to be indistinguishable, then it is meaningless to claim that they agree: we will never be able to perform an experiment to check.

We can estimate the highest SNR for which two waveforms are indistinguishable for a single GW detector as



follows. Choose the binary mass, the detector, and the distance of the source to the detector. Determine the time and phase shift such that the mismatch between the two waveforms is a minimum. Calculate the difference between those two aligned waveforms in the time domain,  $\delta h(t) = h_1(t) - h_2(t)$ , and transform to the frequency domain to produce  $\delta \tilde{h}(f)$ . It was shown in [157] that when the inner product of  $\delta \tilde{h}(f)$  satisfies the criteria

$$\langle \delta \tilde{h} | \delta \tilde{h} \rangle < 1, \quad (16)$$

the two waveforms are indistinguishable. Additional time and phase shifts are applied to  $h_1$  and  $h_2$  such that the left-hand side of Eq. (16) is minimized. This quantity and the SNR are both inversely proportional to the distance of the source to the detector. Therefore, having calculated the SNR and the value of  $\langle \delta \tilde{h} | \delta \tilde{h} \rangle$  for one source distance, we may immediately estimate the maximum SNR such that the inequality in Eq. (16) is satisfied. The results of this calculation are shown in Fig. 9.

This analysis applies to any estimation of the *intrinsic* parameters of the binary, like the total mass and mass ratio. But we should emphasize that, since we minimized

$\langle \delta \tilde{h} | \delta \tilde{h} \rangle$  with respect to a phase and time shift, Fig. 9 does not apply to an estimation of the signal's time of arrival or phase, or parameters that rely on them (like the sky location). It should also be emphasized that our analysis is restricted to parameter estimation based on the output of only one detector.

Note also that the relative performance of each waveform is not necessarily the same for both the detection and measurement analyses. This is because the match calculation finds the best agreement in phase only, while the measurement calculation locates the best match in phase *and* amplitude.

We can estimate from Fig. 9 that the SpEC, BAM, CCATIE, and MayaKranc waveforms will be indistinguishable according to Eq. (16) if the SNR is below about 25; if the Hahndol waveform is to also be indistinguishable, the SNR must be below 14.

SNRs above 25 are expected to be uncommon for the Enhanced LIGO and Virgo detectors; for example, in the NINJA study, numerical waveforms were injected into simulated detector noise at SNRs no higher than 30 [82]. For the Advanced LIGO and Virgo detectors, however,

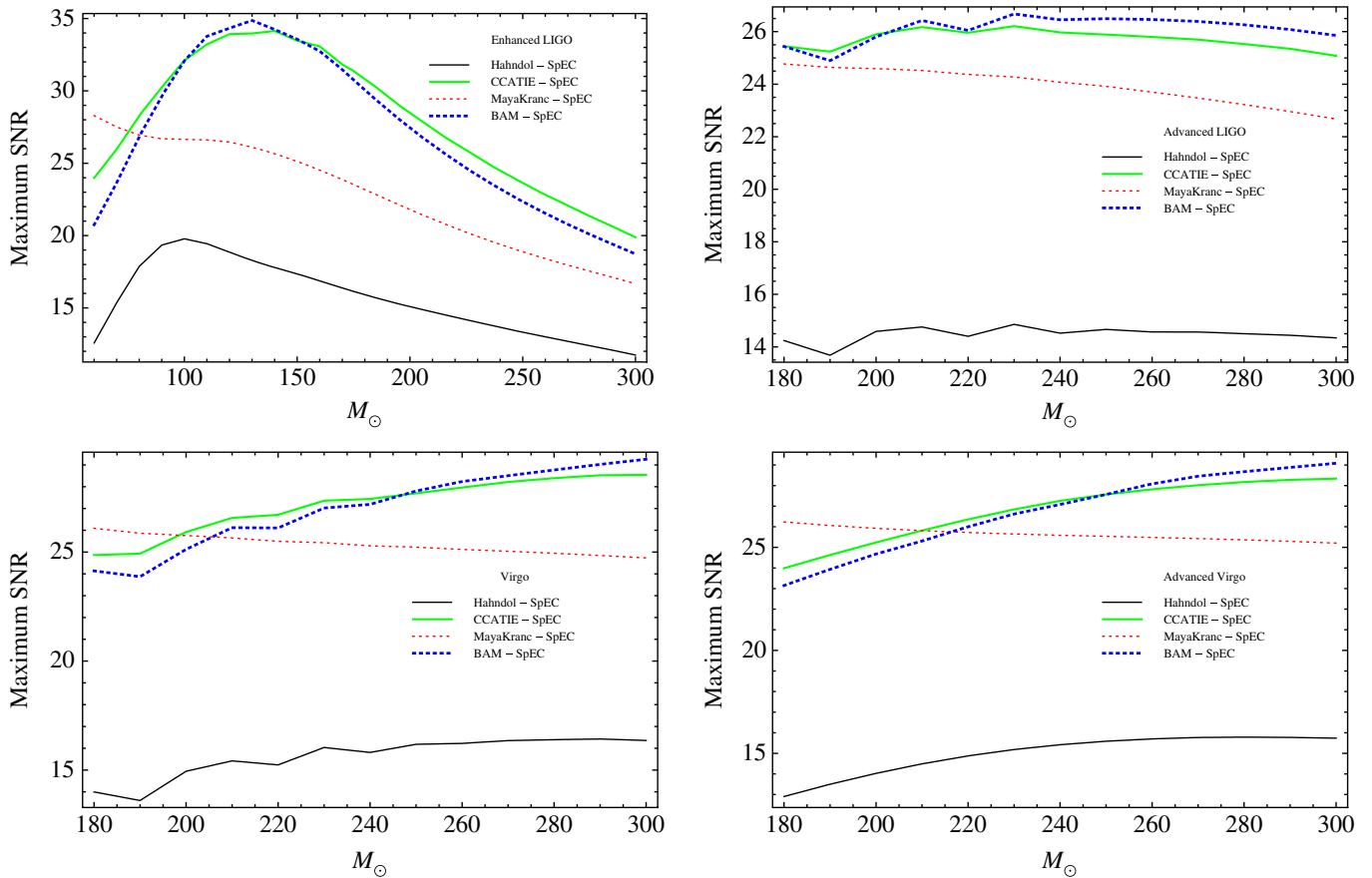


FIG. 9 (color online). The SNR below which the SpEC and all other waveforms will be indistinguishable in any measurement of parameters. Results are shown for the Enhanced LIGO, Advanced LIGO, Virgo, and Advanced Virgo detectors. See text for further explanation.

which have roughly 10 times the range, SNRs in excess of 25 are far more likely.

## V. CONCLUSION

We have compared numerical-relativity waveforms for the last six orbits, merger, and ringdown of an equal-mass nonspinning binary with minimal eccentricity, as produced by five different computer codes. We focused on the ( $\ell = 2$ ,  $m = 2$ ) mode. The purpose was to perform a stringent consistency check of the results from these codes. We verified that accuracy in the waveform phase and amplitude for each code was consistent with the uncertainty estimates originally published with each waveform.

We also calculated the best mismatch between the most accurate waveform (calculated with the `SpEC` code) and each of the others, for the Enhanced LIGO, Advanced LIGO, Virgo, and Advanced Virgo detectors, and found that it was below  $10^{-3}$  in all cases, and below  $2 \times 10^{-4}$  in the best cases. Recall that the criteria such that no more than 10% of signals is lost is 0.005 (assuming a standard template-bank spacing).

Finally, we calculated the maximum SNR below which the signals would be indistinguishable if observed in the Enhanced LIGO, Advanced LIGO, Virgo, or Advanced Virgo detectors. For the best cases this is about 25, and it is never lower than 14. This suggests that these numerical waveforms are more than adequate as ingredients in template banks for GW searches and parameter estimation (of intrinsic parameters, at least) with the Enhanced LIGO and Virgo detectors, for which a SNR above 25 is unlikely. The `Hahndol` waveform is distinguishable from the others at a SNR of only 14, in which case a more detailed study would be necessary to compare its parameter estimation fidelity with the other waveforms. Nonetheless, we estimate that *less* accurate waveforms would not be desirable for GW data-analysis purposes. We expect that these results extend to other numerical waveforms, *if* they exhibit similar or better levels of numerical uncertainty.

An important caveat to the above statements is that these waveforms could only be used “as is” in detector searches for high-mass binaries. Detection of binaries with lower masses would require waveforms that are longer (extend to lower frequencies), for example, by combining analytic approximations [usually post-Newtonian and effective-one-body (EOB) waveforms] with numerical results. Methods have been proposed to produce both hybrid waveforms [40,78–80,147] and analytic waveforms based on either a phenomenological ansatz [78–80] or the adjustment of free parameters in various EOB prescriptions [39,49,59,68,163,164]. It is the accuracy of those “complete” waveforms that will be important in lower-mass searches, and one may also find that sufficiently accurate complete waveforms will require either much longer numerical waveforms as input, or more physically accurate approximation techniques. Such questions are beyond the

scope of this paper, but are an important topic for future work.

Furthermore, for general waveforms, higher spherical-harmonic modes will play a much more important role, in particular, for parameter estimation. This has first been pointed out for ground-based detectors [165] using post-Newtonian inspiral waveforms, with much recent work on ground-based detectors [166] as well as on the planned space-based LISA mission [10,11]; see e.g. [167–169]. Recently, significant improvements in parameter estimation for LISA from higher mode contributions have also been hinted at for numerical waveforms [170,171]. Large values of the SNR will be typical for future generations of ground-based detectors, and even more so for LISA detections. This will make it possible to determine source parameters far more accurately than with current ground-based detectors, which will in turn place more stringent accuracy requirements on numerical waveforms. However, we hope that by the time LISA flies (2018+), and by the time second and third generation ground-based interferometers are in operation, the typical accuracy of numerical waveforms will have far surpassed that of those considered in this study. Our more immediate concern is whether current numerical codes are producing waveforms of sufficient numerical and physical accuracy for use in current data-analysis applications, and our results suggest that they are, at least as far as one is concerned with the quadrupole mode, which is typically the basis of current matched-filter searches.

## ACKNOWLEDGMENTS

The authors thank Badri Krishnan for the Enhanced LIGO noise curve, as provided by Rana Adhikari on behalf of the LIGO Scientific Collaboration, and Giovanni Losurdo for providing the Advanced Virgo noise curve on behalf of the Virgo Collaboration; Ben Owen and Alberto Vecchio for helpful comments on the manuscript; and Doreen Müller for alerting us to a mislabeling of Fig. 4. M. Hannam was supported by SFI Grant No. 07/RFP/PHYF148, and thanks the Albert Einstein Institute in Potsdam for hospitality while some of this work was carried out. S. Husa has been supported in part by VESF and the European Gravitational Observatory (EGO), by DAAD Grant No. D/07/13385, and by Grant No. FPA-2007-60220 from the Spanish Ministerio de Educación y Ciencia. B. Kelly was supported by the NASA Postdoctoral Program at the Oak Ridge Associated Universities. F. Herrmann, I. Hinder, P. Laguna, and D. Shoemaker acknowledge the support of the Center for Gravitational Wave Physics at Penn State funded by the National Science Foundation under Cooperative Agreement No. PHY-0114375. P. Laguna and D. Shoemaker were also supported by NSF Grant No. PHY-0653443, No. PHY-065303, and No. PHY-0555436. F. Herrmann was also supported by NSF Grant No. PHY-0801213. J.

Baker, M. Boyle, M. Hannam, F. Herrmann, S. Husa, L. Kidder, H. Pfeiffer, and M. Scheel thank the Kavli Institute for Theoretical Physics (KITP) Santa Barbara for hospitality during the workshop “Interplay between Numerical Relativity and Data Analysis,” where this work was initiated; the Kavli Institute is supported by NSF Grant No. PHY05-51164. BAM simulations were carried out at LRZ Munich. CCATIE simulations were supported by Teragrid Grant No. TG-MCA02N014. Hahndol simulations were carried out using Project Columbia at NASA Ames Research Center. Some of the SPEC simulations discussed here were produced with LIGO Laboratory computing facilities. LIGO was constructed by the California

Institute of Technology and Massachusetts Institute of Technology with funding from the National Science Foundation, and operates under Cooperative Agreement No. PHY-0107417. This work was supported in part by the DFG Grant No. SFB/Transregio 7 “Gravitational Wave Astronomy”; by grants from the Sherman Fairchild Foundation to Caltech and Cornell, and from the Brinson Foundation to Caltech; by NSF Grant No. PHY-0601459, No. PHY-0652995, No. DMS-0553302, and NASA Grant No. NNG05GG52G at Caltech; by NSF Grant No. PHY-0652952, No. DMS-0553677, No. PHY-0652929, and NASA Grant No. NNG05GG51G at Cornell; and by NASA Grant No. O5-BEFS-05-0044 at Goddard.

- 
- [1] B. Abbott *et al.* (LIGO Scientific Collaboration), arXiv:0711.3041.
- [2] S. Waldman (LIGO Scientific Collaboration), *Classical Quantum Gravity* **23**, S653 (2006).
- [3] LIGO, <http://www.ligo.caltech.edu/>.
- [4] F. Acernese *et al.*, *Classical Quantum Gravity* **23**, S635 (2006).
- [5] Virgo, <http://www.virgo.infn.it/>.
- [6] K. Danzmann, *Lect. Notes Phys.* **410**, 184 (1992).
- [7] S. Hild (LIGO Scientific Collaboration), *Classical Quantum Gravity* **23**, S643 (2006).
- [8] GEO600, <http://geo600.aei.mpg.de/>.
- [9] S. A. Hughes, arXiv:0711.0188.
- [10] K. Danzmann, P. Bender, A. Brillet, I. C. A. Cruise, C. Cutler, F. Fidecaro, W. Folkner, J. Hough, P. McNamara, M. Peterseim *et al.*, Max-Planck-Institut für Quantenoptik Report No. MPQ 233, 1998.
- [11] K. Danzmann and A. Rüdiger, *Classical Quantum Gravity* **20**, S1 (2003).
- [12] L. Blanchet, *Living Rev. Relativity* **9**, 4 (2006), <http://www.livingreviews.org/lrr-2006-4>.
- [13] K. D. Kokkotas and B. G. Schmidt, *Living Rev. Relativity* **2**, 2 (1999), <http://www.livingreviews.org/lrr-1999-2>.
- [14] F. Pretorius, *Phys. Rev. Lett.* **95**, 121101 (2005).
- [15] M. Campanelli, C. O. Lousto, P. Marronetti, and Y. Zlochower, *Phys. Rev. Lett.* **96**, 111101 (2006).
- [16] J. G. Baker, J. Centrella, D.-I. Choi, M. Koppitz, and J. van Meter, *Phys. Rev. Lett.* **96**, 111102 (2006).
- [17] P. Diener, F. Herrmann, D. Pollney, E. Schnetter, E. Seidel, R. Takahashi, J. Thornburg, and J. Ventrella, *Phys. Rev. Lett.* **96**, 121101 (2006).
- [18] M. Campanelli, C. O. Lousto, Y. Zlochower, B. Krishnan, and D. Merritt, *Phys. Rev. D* **75**, 064030 (2007).
- [19] M. Campanelli, C. O. Lousto, and Y. Zlochower, *Phys. Rev. D* **74**, 084023 (2006).
- [20] M. Campanelli, C. O. Lousto, and Y. Zlochower, *Phys. Rev. D* **74**, 041501(R) (2006).
- [21] M. Campanelli, C. O. Lousto, and Y. Zlochower, *Phys. Rev. D* **73**, 061501(R) (2006).
- [22] M. A. Scheel *et al.*, *Phys. Rev. D* **74**, 104006 (2006).
- [23] J. A. Gonzalez, U. Sperhake, B. Brügmann, M. Hannam, and S. Husa, *Phys. Rev. Lett.* **98**, 091101 (2007).
- [24] J. G. Baker, S. T. McWilliams, J. R. van Meter, J. Centrella, D.-I. Choi, B. J. Kelly, and M. Koppitz, *Phys. Rev. D* **75**, 124024 (2007).
- [25] J. G. Baker, J. R. van Meter, S. T. McWilliams, J. Centrella, and B. J. Kelly, *Phys. Rev. Lett.* **99**, 181101 (2007).
- [26] J. G. Baker *et al.*, *Astrophys. J.* **653**, L93 (2006).
- [27] J. G. Baker, J. Centrella, D.-I. Choi, M. Koppitz, and J. van Meter, *Phys. Rev. D* **73**, 104002 (2006).
- [28] U. Sperhake, *Phys. Rev. D* **76**, 104015 (2007).
- [29] P. Marronetti, W. Tichy, B. Brügmann, J. González, and U. Sperhake, *Phys. Rev. D* **77**, 064010 (2008).
- [30] L. Lindblom, K. D. Matthews, O. Rinne, and M. A. Scheel, *Phys. Rev. D* **77**, 084001 (2008).
- [31] M. Boyle *et al.*, *Phys. Rev. D* **76**, 124038 (2007).
- [32] H. P. Pfeiffer *et al.*, *Classical Quantum Gravity* **24**, S59 (2007).
- [33] W. Tichy and P. Marronetti, *Phys. Rev. D* **76**, 061502 (2007).
- [34] I. Hinder, B. Vaishnav, F. Herrmann, D. Shoemaker, and P. Laguna, *Phys. Rev. D* **77**, 081502 (2008).
- [35] F. Herrmann, I. Hinder, D. Shoemaker, and P. Laguna, *Classical Quantum Gravity* **24**, S33 (2007).
- [36] F. Herrmann, I. Hinder, D. M. Shoemaker, P. Laguna, and R. A. Matzner, *Phys. Rev. D* **76**, 084032 (2007).
- [37] B. Vaishnav, I. Hinder, F. Herrmann, and D. Shoemaker, *Phys. Rev. D* **76**, 084020 (2007).
- [38] J. D. Schnittman *et al.*, *Phys. Rev. D* **77**, 044031 (2008).
- [39] A. Buonanno *et al.*, *Phys. Rev. D* **76**, 104049 (2007).
- [40] Y. Pan *et al.*, *Phys. Rev. D* **77**, 024014 (2008).
- [41] J. G. Baker *et al.*, *Astrophys. J.* **668**, 1140 (2007).
- [42] D.-I. Choi *et al.*, *Phys. Rev. D* **76**, 104026 (2007).
- [43] C. O. Lousto and Y. Zlochower, *Phys. Rev. D* **77**, 044028 (2008).
- [44] M. Campanelli, C. O. Lousto, Y. Zlochower, and D. Merritt, *Phys. Rev. Lett.* **98**, 231102 (2007).
- [45] M. Campanelli, C. O. Lousto, Y. Zlochower, and D. Merritt, *Astrophys. J.* **659**, L5 (2007).

- [46] E. Berti, V. Cardoso, J. A. Gonzalez, U. Sperhake, and B. Brügmann, *Classical Quantum Gravity* **25**, 114035 (2008).
- [47] U. Sperhake *et al.*, *Phys. Rev. D* **78**, 064069 (2008).
- [48] L. Rezzolla *et al.*, *Phys. Rev. D* **78**, 044002 (2008).
- [49] T. Damour, A. Nagar, E. N. Dorband, D. Pollney, and L. Rezzolla, *Phys. Rev. D* **77**, 084017 (2008).
- [50] L. Rezzolla *et al.*, *Astrophys. J.* **679**, 1422 (2008).
- [51] D. Pollney *et al.*, *Phys. Rev. D* **76**, 124002 (2007).
- [52] M. Koppitz *et al.*, *Phys. Rev. Lett.* **99**, 041102 (2007).
- [53] M. Hannam, S. Husa, B. Brügmann, and A. Gopakumar, *Phys. Rev. D* **78**, 104007 (2008).
- [54] B. Brügmann, J. A. Gonzalez, M. Hannam, S. Husa, and U. Sperhake, *Phys. Rev. D* **77**, 124047 (2008).
- [55] M. Hannam, S. Husa, J. A. González, U. Sperhake, and B. Brügmann, *Phys. Rev. D* **77**, 044020 (2008).
- [56] S. Husa, M. Hannam, J. A. Gonzalez, U. Sperhake, and B. Brügmann, *Phys. Rev. D* **77**, 044037 (2008).
- [57] S. Husa, J. A. Gonzalez, M. Hannam, B. Brügmann, and U. Sperhake, *Classical Quantum Gravity* **25**, 105006 (2008).
- [58] J. A. González, M. D. Hannam, U. Sperhake, B. Brügmann, and S. Husa, *Phys. Rev. Lett.* **98**, 231101 (2007).
- [59] T. Damour, A. Nagar, M. Hannam, S. Husa, and B. Brügmann, *Phys. Rev. D* **78**, 044039 (2008).
- [60] B. Brügmann *et al.*, *Phys. Rev. D* **77**, 024027 (2008).
- [61] M. A. Scheel *et al.*, *Phys. Rev. D* **79**, 024003 (2009).
- [62] M. Boyle *et al.*, *Phys. Rev. D* **78**, 104020 (2008).
- [63] W. Tichy and P. Marronetti, *Phys. Rev. D* **78**, 081501 (2008).
- [64] J. Healy *et al.*, *Phys. Rev. Lett.* **102**, 041101 (2009).
- [65] I. Hinder, F. Herrmann, P. Laguna, and D. Shoemaker, arXiv:0806.1037.
- [66] D. Shoemaker, B. Vaishnav, I. Hinder, and F. Herrmann, *Classical Quantum Gravity* **25**, 114047 (2008).
- [67] M. C. Washik *et al.*, *Phys. Rev. Lett.* **101**, 061102 (2008).
- [68] J. G. Baker *et al.*, *Phys. Rev. D* **78**, 044046 (2008).
- [69] J. G. Baker *et al.*, *Astrophys. J.* **682**, L29 (2008).
- [70] M. Campanelli, C. O. Lousto, H. Nakano, and Y. Zlochower, arXiv:0808.0713 [Phys. Rev. D (to be published)].
- [71] C. O. Lousto and Y. Zlochower, *Phys. Rev. D* **79**, 064018 (2009).
- [72] S. Dain, C. O. Lousto, and Y. Zlochower, *Phys. Rev. D* **78**, 024039 (2008).
- [73] U. Sperhake, V. Cardoso, F. Pretorius, E. Berti, and J. A. Gonzalez, *Phys. Rev. Lett.* **101**, 161101 (2008).
- [74] Z. Cao, H.-J. Yo, and J.-P. Yu, *Phys. Rev. D* **78**, 124011 (2008).
- [75] J. A. Gonzalez, U. Sperhake, and B. Brügmann, arXiv:0811.3952.
- [76] B. Walther, B. Brügmann, and D. Mueller, arXiv:0901.0993.
- [77] M. Shibata, H. Okawa, and T. Yamamoto, *Phys. Rev. D* **78**, 101501 (2008).
- [78] P. Ajith, S. Babak, Y. Chen, M. Hewitson, B. Krishnan, J. T. Whelan, B. Brügmann, P. Diener, J. González, M. Hannam *et al.*, *Classical Quantum Gravity* **24**, S689 (2007).
- [79] P. Ajith *et al.*, *Phys. Rev. D* **77**, 104017 (2008).
- [80] P. Ajith, *Classical Quantum Gravity* **25**, 114033 (2008).
- [81] LSC Algorithm Library, <http://www.lsc-group.phys.uwm.edu/lal>.
- [82] B. Aylott *et al.*, arXiv:0901.4399.
- [83] J. G. Baker, M. Campanelli, F. Pretorius, and Y. Zlochower, *Classical Quantum Gravity* **24**, S25 (2007).
- [84] B. Brügmann, J. A. González, M. Hannam, S. Husa, U. Sperhake, and W. Tichy, *Phys. Rev. D* **77**, 024027 (2008).
- [85] S. Husa, J. A. González, M. Hannam, B. Brügmann, and U. Sperhake, *Classical Quantum Gravity* **25**, 105006 (2008).
- [86] B. Imbiriba, J. Baker, D.-I. Choi, J. Centrella, D. R. Fiske, J. D. Brown, J. R. van Meter, and K. Olson, *Phys. Rev. D* **70**, 124025 (2004).
- [87] J. R. van Meter, J. G. Baker, M. Koppitz, and D.-I. Choi, *Phys. Rev. D* **73**, 124011 (2006).
- [88] M. Shibata and T. Nakamura, *Phys. Rev. D* **52**, 5428 (1995).
- [89] T. W. Baumgarte and S. L. Shapiro, *Phys. Rev. D* **59**, 024007 (1998).
- [90] M. Alcubierre, B. Brügmann, P. Diener, M. Koppitz, D. Pollney, E. Seidel, and R. Takahashi, *Phys. Rev. D* **67**, 084023 (2003).
- [91] M. Hannam, S. Husa, D. Pollney, B. Brügmann, and N. O’Murchadha, *Phys. Rev. Lett.* **99**, 241102 (2007).
- [92] C. Gundlach and J. M. Martin-Garcia, *Phys. Rev. D* **74**, 024016 (2006).
- [93] H. Friedrich and A. D. Rendall, *Lect. Notes Phys.* **540**, 127 (2000).
- [94] L. Lindblom, M. A. Scheel, L. E. Kidder, R. Owen, and O. Rinne, *Classical Quantum Gravity* **23**, S447 (2006).
- [95] J. Baker, M. Campanelli, C. O. Lousto, and R. Takahashi, *Phys. Rev. D* **65**, 124012 (2002).
- [96] M. Alcubierre, B. Brügmann, P. Diener, F. S. Guzmán, I. Hawke, S. Hawley, F. Herrmann, M. Koppitz, D. Pollney, E. Seidel *et al.*, *Phys. Rev. D* **72**, 044004 (2005).
- [97] E. Berti, V. Cardoso, and C. M. Will, *Phys. Rev. D* **73**, 064030 (2006).
- [98] B. Abbott *et al.* (LIGO Scientific Collaboration), *Phys. Rev. D* **77**, 062002 (2008).
- [99] C. Cutler and K. S. Thorne, “An Overview of Gravitational-wave Sources,” in *Proceedings of the 16th International Conference on General Relativity and Gravitation, Durban, South Africa, 2001*, edited by N. T. Bishop and S. D. Maharaj (World Scientific, Singapore, 2002).
- [100] V. Kalogera, K. Belczynski, C. Kim, R. O’Shaughnessy, and B. Willems, *Phys. Rep.* **442**, 75 (2007).
- [101] K. Belczynski, V. Kalogera, F. A. Rasio, R. E. Taam, and T. Bulik, *Astrophys. J.* **662**, 504 (2007).
- [102] A. Sadowski *et al.*, arXiv:0710.0878.
- [103] R. Adhikari, P. Fritschel, and S. Waldman (LIGO Scientific Collaboration), Technical Report No. LIGO-T060156-01-I, 2006, <http://www.ligo.caltech.edu/docs/T/T060156-01.pdf>.
- [104] Advanced LIGO, <http://www.ligo.caltech.edu/advLIGO/>.
- [105] F. R. *et al.* (Virgo Collaboration), Technical Report No. VIR-NOT-DIR-1390-304, 2005.
- [106] K. Postnov and L. Yungelson, *Living Rev. Relativity* **9**, 6 (2006), <http://www.livingreviews.org/lrr-2006-6>.
- [107] M. J. Benacquista, *Living Rev. Relativity* **9**, 2 (2006), <http://www.livingreviews.org/lrr-2006-2>.



- [108] M. Volonteri, P. Madau, E. Quataert, and M.J. Rees, *Astrophys. J.* **620**, 69 (2005).
- [109] C.F. Gammie, S.L. Shapiro, and J.C. McKinney, *Astrophys. J.* **602**, 312 (2004).
- [110] S.L. Shapiro, *Astrophys. J.* **620**, 59 (2005).
- [111] P.C. Peters, *Phys. Rev.* **136**, B1224 (1964).
- [112] S. Brandt and B. Brügmann, *Phys. Rev. Lett.* **78**, 3606 (1997).
- [113] J.M. Bowen and J.W. York, Jr., *Phys. Rev. D* **21**, 2047 (1980).
- [114] R. Beig and N. O’Murchadha, *Classical Quantum Gravity* **11**, 419 (1994).
- [115] R. Beig and S. Husa, *Phys. Rev. D* **50**, R7116 (1994).
- [116] S. Dain and H. Friedrich, *Commun. Math. Phys.* **222**, 569 (2001).
- [117] M. Ansorg, B. Brügmann, and W. Tichy, *Phys. Rev. D* **70**, 064011 (2004).
- [118] M. Hannam, S. Husa, N. Ó. Murchadha, B. Brügmann, J. A. González, and U. Sperhake, *J. Phys. Conf. Ser.* **66**, 012047 (2007).
- [119] M. Hannam, S. Husa, F. Ohme, B. Brügmann, and N. Ó Murchadha, *Phys. Rev. D* **78**, 064020 (2008).
- [120] J.D. Brown, *Phys. Rev. D* **77**, 044018 (2008).
- [121] J.W. York, *Phys. Rev. Lett.* **82**, 1350 (1999).
- [122] H.P. Pfeiffer and J.W. York, *Phys. Rev. D* **67**, 044022 (2003).
- [123] G.B. Cook, *Phys. Rev. D* **65**, 084003 (2002).
- [124] G.B. Cook and H.P. Pfeiffer, *Phys. Rev. D* **70**, 104016 (2004).
- [125] M. Caudill, G.B. Cook, J.D. Grigsby, and H.P. Pfeiffer, *Phys. Rev. D* **74**, 064011 (2006).
- [126] C. Bona, J. Massó, E. Seidel, and J. Stela, *Phys. Rev. D* **56**, 3405 (1997).
- [127] H. Friedrich, *Commun. Math. Phys.* **100**, 525 (1985).
- [128] C. Gundlach, J.M. Martin-Garcia, G. Calabrese, and I. Hinder, *Classical Quantum Gravity* **22**, 3767 (2005).
- [129] F. Pretorius, *Classical Quantum Gravity* **22**, 425 (2005).
- [130] O. Rinne, *Classical Quantum Gravity* **23**, 6275 (2006).
- [131] O. Rinne, L. Lindblom, and M.A. Scheel, *Classical Quantum Gravity* **24**, 4053 (2007).
- [132] J.M. Stewart, *Classical Quantum Gravity* **15**, 2865 (1998).
- [133] H. Friedrich and G. Nagy, *Commun. Math. Phys.* **201**, 619 (1999).
- [134] J. Bardeen and L. Buchman, *Phys. Rev. D* **65**, 064037 (2002).
- [135] B. Szilágyi, B. Schmidt, and J. Winicour, *Phys. Rev. D* **65**, 064015 (2002).
- [136] G. Calabrese, J. Pullin, O. Reula, O. Sarbach, and M. Tiglio, *Commun. Math. Phys.* **240**, 377 (2003).
- [137] B. Szilágyi and J. Winicour, *Phys. Rev. D* **68**, 041501 (2003).
- [138] L.E. Kidder, L. Lindblom, M.A. Scheel, L.T. Buchman, and H.P. Pfeiffer, *Phys. Rev. D* **71**, 064020 (2005).
- [139] L.T. Buchman and O.C.A. Sarbach, *Classical Quantum Gravity* **23**, 6709 (2006).
- [140] D. Gottlieb and J.S. Hesthaven, *J. Comput. Appl. Math.* **128**, 83 (2001).
- [141] J.S. Hesthaven, *Applied Numerical Mathematics* **33**, 23 (2000).
- [142] E.T. Newman and R. Penrose, *J. Math. Phys. (N.Y.)* **3**, 566 (1962); **4**, 998(E) (1963).
- [143] J.M. Stewart, *Advanced General Relativity* (Cambridge University Press, Cambridge, England, 1990).
- [144] S.A. Teukolsky, *Astrophys. J.* **185**, 635 (1973).
- [145] A. Nagar and L. Rezzolla, *Classical Quantum Gravity* **22**, R167 (2005); **23**, 4297(E) (2006).
- [146] E. Berti *et al.*, *Phys. Rev. D* **76**, 064034 (2007).
- [147] M. Boyle, D.A. Brown, and L. Pekowsky, arXiv:0901.1628.
- [148] A. Buonanno, G.B. Cook, and F. Pretorius, *Phys. Rev. D* **75**, 124018 (2007).
- [149] L. Blanchet, T. Damour, G. Esposito-Farese, and B.R. Iyer, *Phys. Rev. Lett.* **93**, 091101 (2004).
- [150] L. Lehner and O.M. Moreschi, *Phys. Rev. D* **76**, 124040 (2007).
- [151] B.J. Owen, *Phys. Rev. D* **53**, 6749 (1996).
- [152] C. Cutler and E.E. Flanagan, *Phys. Rev. D* **49**, 2658 (1994).
- [153] T. Damour, B.R. Iyer, and B.S. Sathyaprakash, *Phys. Rev. D* **57**, 885 (1998).
- [154] B. Abbott *et al.* (LIGO Scientific Collaboration), *Phys. Rev. D* **69**, 122001 (2004).
- [155] B. Abbott *et al.* (LIGO Scientific Collaboration), *Phys. Rev. D* **72**, 082001 (2005).
- [156] B. Abbott *et al.* (LIGO Scientific Collaboration), *Phys. Rev. D* **73**, 102002 (2006).
- [157] L. Lindblom, B.J. Owen, and D.A. Brown, *Phys. Rev. D* **78**, 124020 (2008).
- [158] L.S. Finn, *Phys. Rev. D* **46**, 5236 (1992).
- [159] L.S. Finn and D.F. Chernoff, *Phys. Rev. D* **47**, 2198 (1993).
- [160] C. Cutler and M. Vallisneri, *Phys. Rev. D* **76**, 104018 (2007).
- [161] F. Beauville *et al.* (LIGO/Virgo Working Group), *Classical Quantum Gravity* **25**, 045001 (2008).
- [162] B. Abbott *et al.* (LIGO Scientific Collaboration), *Classical Quantum Gravity* **25**, 245008 (2008).
- [163] T. Damour and A. Nagar, *Phys. Rev. D* **77**, 024043 (2008).
- [164] A.H. Mroue, L.E. Kidder, and S.A. Teukolsky, *Phys. Rev. D* **78**, 044004 (2008).
- [165] A.M. Sintes and A. Vecchio, in *Proceedings of the 34th Rencontres de Moriond: Gravitational Waves and Experimental Gravity, Les Arcs, France, 1999* (Editions Frontières, Gif-sur-Yvette, France, 1999).
- [166] C. Van Den Broeck and A.S. Sengupta, *Classical Quantum Gravity* **24**, 1089 (2007).
- [167] K.G. Arun, B.R. Iyer, B.S. Sathyaprakash, S. Sinha, and C.V.D. Broeck, *Phys. Rev. D* **76**, 104016 (2007).
- [168] M. Trias and A.M. Sintes, *Phys. Rev. D* **77**, 024030 (2008).
- [169] K.G. Arun *et al.*, arXiv:0811.1011.
- [170] S. Babak, M. Hannam, S. Husa, and B. Schutz, arXiv:0806.1591.
- [171] J.I. Thorpe *et al.*, arXiv:0811.0833.